Properties of 3D-printed fiber-reinforced Portland cement paste

Manuel Hambach, Dirk Volkmer*

Chair of Solid State and Materials Chemistry, University of Augsburg, Augsburg 86159, Germany

1. Introduction

Regular Portland cement-based construction materials exhibit a high compressive strength (around 20–60 MPa for general usage) [1], but they fall short in terms of tensile and flexural strength values (3–10 MPa) for plain cement pastes [2,3]. As a common solution, steel-reinforcement is placed in the formworks in order to improve flexural strength of the cementitious composite. However, steel-reinforcement is resulting in time- and material-consuming labor costs during the construction process since the steel has to be placed and fixed by hand in construction molds. To avoid the disadvantages of steel-reinforcement, mortars and concretes containing high performance synthetic fibers (e.g. glass or carbon fibers), were introduced in the 1960s in the scientific literature [4]. The resulting composite materials show a remarkable increase in flexural and tensile properties leading to an ultimate flexural strength of up to 50 MPa – one order of magnitude higher than the corresponding value for plain concrete (without further reinforcement) [5–7]. Since the late 1990s efforts have been made on extruding fiber-reinforced cement pastes in a simple extrusion process, in order to increase the density of the cement paste and to influence, to a certain extent, also the orientation of fibers in the cementitious matrix [8–11]. Employing fiber alignment in the cement paste upon pressing the cementitious paste through a small extrusion nozzle, high flexural strength values of fiber-reinforced composites up to 120 MPa can be achieved [12]. Since extrusion techniques, forcing fiber alignment, are capable to produce high performance fiber-reinforced cementitious composites, the next technological step should head towards automated layer based fabrication, nowadays known as *additive manufacturing* or *3D-printing*, and has already been introduced into the manufacturing of cement-based materials [13–15]. Similar developments towards 3D-printing can also be observed in related materials classes, e.g. biomedical materials [16,17], polymer composites [18,19] or bone replacement materials [20–24].

3D-printing is a technique first introduced in the late 1980s, which is gaining more and more importance in production processes during recent years [25], since it enables the fabrication of complex, multiscale structures through computer-aided design (CAD) [26,27]. Continuous extrusion or FDM (fused deposition modelling) is based on extruding a (semi-)liquid paste, typically a molten thermoplastic polymer, and depositing the material by a computer-controlled extrusion system [28]. In this report we apply FDM 3D-printing on cementitious materials by storing the ready-mixed paste in a reservoir and extruding the material, by a movable piston system of a dispenser, in order to form layered structures. However, the need of steel reinforcement currently hampers the fully-automated processing of free-formed 3D constructions structures made from Portland cement-based materials. As a possible solution, common steel-reinforced concrete might be substituted by a 3D-printable short carbon fiber-reinforced cement exhibiting high flexural strength, thus minimizing the content of

* Corresponding author.
E-mail address: dirk.volkmer@physik.uni-augsburg.de (D. Volkmer).

reinforcement steel in load bearing structures. In the following we describe the required materials development in conjunction with a suitable 3D printing approach, which point into this direction.

2. Experimental

Fiber treatment: To provide good fiber dispersion [29] and fiber bonding to the cementitious matrix [30,31], all fibers were heat-treated to remove the fibers' sizing and to ensure a hydrophilic fiber surface. For carbon fibers a 400 °C and for glass and basalt fibers a 500 °C thermal treatment ensures the removing of the polymer sizing, as illustrated in Supplementary Fig. S1.

Cement paste preparation: For 3D-printing 61.5 % by weight of type I 52.5 R Portland cement (Schwenk Zement KG) was used along with 21 % by weight of silica fume (Microsil, Elkem), 15 % by weight of water and 2.5 % by weight of a water reducing agent (Glenium ACE 430, BASF). The water cement ratio was 0.3 (including water reducing agent). To avoid thickening of the cement paste during 3D-printing 0.3 % by weight of a hydration inhibitor (PANTARHOL 85, Pferrer) was added. The infill mortar for hierarchical specimens was prepared from 40.0 % by weight of type I 52.5 R Portland cement and 60.0 % by weight of sand (Gebenbacher Sand) along with a water cement ratio of 0.4. All solid components, apart from reinforcement fibers, were mixed in dry state. Water, water reducing agent, and hydration inhibitor were added and mixed with a rotary mixer at 600 RPM until a homogeneous mixture was obtained. Finally, the reinforcement fibers were added and the mixture was stirred again at 50 RPM until the fibers became uniformly dispersed. Characteristic properties of the reinforcement fibers employed in our studies are presented in Table 1.

3D-printing system and specimen preparation: 3D-objects fitting the desired specimen dimensions were sketched in FreeCAD (build 0.15) CAD-software and a 3D-print preparation software (Cura, build 15.14.02) was used to create g-code print paths. For 3D-printing a DeltaWASP 20 × 40 3D-printer (WASProject) was used along with the WASP Clay Extruder Kit 2.0 having a nozzle 2 mm in diameter attached to the extruder. After (fiber-reinforced) cement paste was mixed, it was immediately filled into the storage container of the 3D-printing system, a pressure of 3 bar was applied on the piston of the storage container and kept constant at this value during specimen printing, which was typically accomplished within 3 h. Best results were obtained by adjusting a layer height of 1.5 mm and a print speed of 30 mm/s.

Specimen storage: After preparation the samples were stored for 24 h in a desiccator providing 100% relative humidity followed by placing the samples for another 6 days in a water bath (about 0.5 l for five specimens). The samples were stored for another 21 days in a desiccator over saturated sodium bromide solution (at 58% relative air humidity). All mechanical tests were immediately performed after a storage period of 28 days. Prior to testing, all specimens were polished in order to obtain clean and parallel object surfaces required for mechanical tests.

Flexural strength measurements: Flexural strength measurements were carried out in a 3-point bending test setup. The testing machine was a Zwick/Roell BT1-FR05TN.D14 with a 500 N or 5 kN load cell attached (depending on specimen dimensions and expected maximum load). By measuring the maximum force F the flexural strength fs can be calculated by the following Equation (1):

$$fs = \frac{3}{2} * \frac{F*l}{w*h^2} \tag{1}$$

where l represents the distance between the supports (50 ± 0.1 mm for specimens 60 mm in length and 100 ± 0.1 mm for specimens 120 mm in length), w is the specimen's width and h is the specimen's height. The specimen's dimensions were determined prior to the measurement within an accuracy of about 0.1 mm.

Compressive strength measurements: For compressive strength measurements at least five specimens for each testing series were tested. A Zwick/Roell BZ1-MM14640.ZW03 testing machine with a 50 kN load cell attached was used. By measuring the maximum force F the compressive strength cs can be calculated by the following Equation (2):

$$cs = \frac{F}{l*w} \tag{2}$$

l represents the length and w the width of the sample. Again, the specimen's dimensions were determined prior to the measurement within an accuracy of 0.1 mm.

Specimen density and helium porosity measurements: The surfaces of each specimen were polished in order to get even and parallel borders required for accurate volume measurement. After storing the specimens for 12 h in an oven at a constant temperature of 130 °C, the specimen density was calculated by determining the specimen's volume (vol_{spec} = length × width × height) within an accuracy of 0.01 mm and the specimen's weight within an accuracy of 0.1 mg. The specimens were then crushed with a Kinematica Polymix PX-MFC 90 D mill in order to measure the specimen's bulk volume (vol_{bulk}) by helium pycnometry with a Micromeritics AccuPyc II 1340. Helium porosity p can be calculated by Equation (3):

$$p = \left(1 - \frac{vol_{bulk}}{vol_{spec}}\right) * 100 \ (vol. - \%) \tag{3}$$

3. Results and discussion

3.1. Properties of 3D-printed fiber-reinforced cement paste

A small scale setup (specimen dimensions up to several centimeters, Fig. 1a) is used to investigate influence of layer orientation, density and porosity on the strength of 3D-printed Portland cement paste. Furthermore, short fibers (carbon-, glass- or basalt fibers) were used to report on the influence of fiber reinforcement on distinct mechanical properties, namely flexural and compressive strength, in 3D-printed fiber-reinforced Portland cement paste. Since filler alignment in 3D-printed structures has previously been employed successfully for polymer composites [18], fiber alignment here is investigated as an efficient means for fiber reinforcement of Portland cement paste. The principle is rather simple: during the

Table 1
Properties of reinforcement fibers used for the present study.

Fiber	Diameter [μm]	Tensile strength [MPa]	Young's modulus [GPa]	Length [mm]	Supplier
Carbon fiber (HT C261)	7	3950	230	3	Toho Tenax
Glass fiber (AR Force D-6)	20	3500	72	6	DuraPact
Basalt fiber (BS 13 0064 12)	13	4200	93	6	Incotelogy

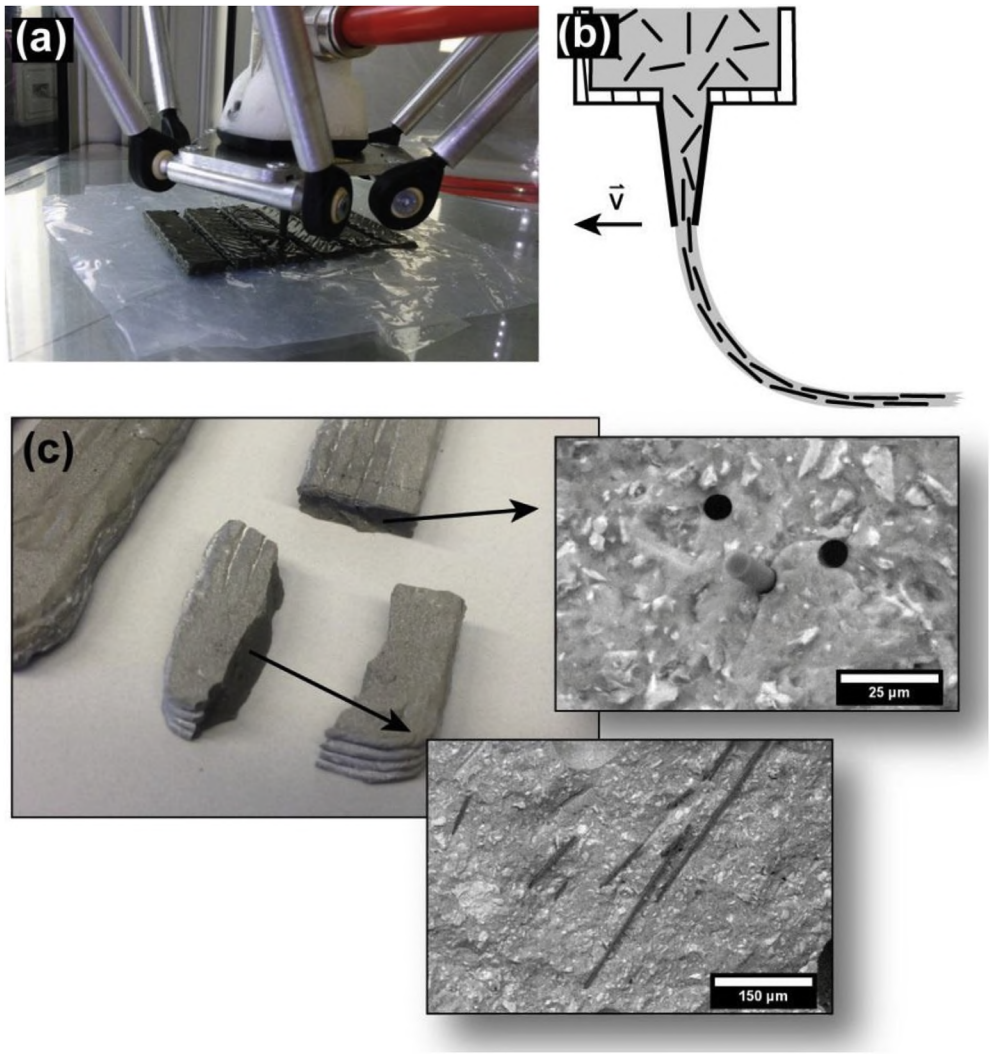

Fig. 1. (a) Photograph of 3D-printing of beam test specimens used in 3-point bending tests (dimensions: 6 × 12 × 60 mm). (b) Schematic illustration of fiber alignment during 3D-printing. (c) Photograph of a sample containing aligned reinforcement fibers and corresponding ESEM micrographs, which show the fiber orientation (perpendicular and parallel to the fracture surface of the specimen).

extrusion process the extrusion nozzle enables fiber alignment along the print path which in turn leads to an increase in flexural/tensile strength of the printed structures in a designated direction (Fig. 1b). To ensure a high degree of aligned fibers, a nozzle diameter (2 mm) being smaller than the average fiber length (3–6 mm) was used after extensive optimization and trial series, employing different ratios of fiber length:nozzle diameters. ESEM micrographs of 3D-printed cement pastes containing reinforcement fibers prove that our prototypic 3D-printing setup leads to strongly aligned carbon-, glass- or basalt fibers in the printed specimens, as shown in Fig. 1c and in the supplementary material (Fig. S2). Thus, the process of alignment of the fibers is used in this study to spatially control mechanical properties, especially flexural/tensile strength, by adjusting the print path directions in the designed structures. Besides mechanical properties, 3D-printing of Portland cement pastes can also influence porosity [13], consequently the porosity of 3D-printed samples is also investigated in this report.

A mixture of 61.5 % by weight of Portland cement, 21 % by weight of Microsilica, 15 % by weight of water and 2.5 % by weight of a water reducing agent was found to exhibit a viscosity low enough to ensure no blockage of the printing nozzle during the printing process. Nevertheless the viscosity was high enough to fabricate stable structures by 3D-printing, which retained their shape until the cement paste was hardened for both plain and fiber-reinforced cement pastes. Attempts to increase the fiber volume content (exceeding about 1.5 vol.-% fibers) caused frequent blocking of the extrusion nozzle, 1 vol.-% of fiber reinforcement was thus used for all specimens' preparations. Cubic specimens (18 mm edge length) and beam specimens (60 mm in length, 12 mm in width and 6 mm in height) were 3D-printed to obtain samples for uniaxial compressive strength tests and 3-point bending tests, respectively. Two different print patterns, namely a parallel shaped (print path A for 3-point bending tests, print path C for uniaxial compressive strength tests) and a crosshatch shaped pattern (print path B for 3-point bending tests, print path D for uniaxial compressive strength tests) were employed (Fig. 2a, b) in order to investigate the influence of different fiber orientations along predetermined print paths. For print path A and C (parallel shape) each layer was printed identical to the layer below and above, for print path B and D (crosshatch shape) each layer was twisted by 90° with respect to the layers beneath and above, resulting in a sandwich-like structure, as illustrated in Fig. 2b and d. Besides fiber-reinforced samples a fiber-free reference was also produced for all print paths reported in the present publication. 3-point bending tests were performed

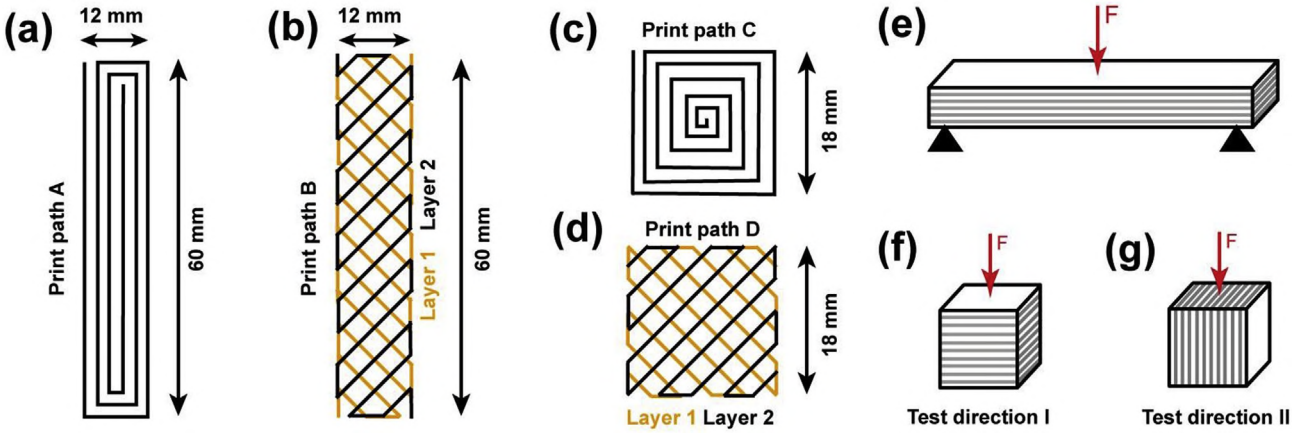

Fig. 2. Top view of the print paths for specimens used for 3-point bending test (a) being parallel printed called "print path A". (b) Illustration of "print path B" samples having 2 different layers (rotated 90° to each other). Top view of print paths for specimens used for uniaxial compressive strength test (c) being parallel printed referred to as "print path C" and (d) being printed in a crosshatch shape called "print path D" (90° rotated to each other layers were used). Schematic illustration of 3D-printed layers (grey lines) and sample orientation in (e) 3-point bending test and (f, g) uniaxial compressive strength test for perpendicular layer orientation referred to as "test direction I" and longitudinal layer orientation referred to as "test direction II".

perpendicular to layer orientation, simulating the most common load case for 3D-printed constructions, as illustrated in Fig. 2e. Compressive strength tests were performed in two directions, perpendicular (test direction I) and longitudinal (test direction II) to the layer orientation, in order to simulate two different load cases for the anisotropic specimens which are obtained in a 3D-printing fabrication process (Fig. 2f, g).

3.1.1. Flexural strength

Flexural strength of the tested beams is ranging from 10 to 30 MPa, depending on reinforcement fiber type and print path. All results are summarized in Table 2 for flexural strength and in the supplementary material (Table S1) for deformation modulus in 3-point bending test. For each testing series at least 5 specimens were tested. 3D-models and photographs of the prepared test specimens are shown in Fig. 3a and b.

Samples printed via print path A exhibit a flexural strength of about 10 MPa, when plain cement paste is being used, and about 13 MPa if glass- or basalt fibers are present. A carbon-fiber reinforced test specimen, in contrast, shows a remarkable increase of strength (30 MPa). Thus, the appropriate selection of different fiber types exerts a strong influence on the flexural strength of the test specimens. Stress-deformation diagrams show that plain and carbon fiber-reinforced samples do not show post-cracking characteristics (Fig. 3c) [32]. In contrast, glass- and basalt fiber samples reveal post-cracking behavior, since stress-deformation curves, provided in the supplementary material (Fig. S3), show residual stress after specimen failure [33,34]. Toughening behavior has been reported for fiber-reinforced concretes [12,35,36] and high performance biomaterials [37,38], characterized by a remarkable zone of plastic deformation ensuring high flexural strength values. A similar behavior can be observed for carbon fiber-reinforced cement paste processed by print path A, which exhibits the highest flexural strength values in combination with significant plastic deformation, ranging from 0.1 to 0.4% deformation, as shown in Fig. 3c. If plain cement paste is being used, samples fabricated with print path A and B did not show different flexural strength. In both cases (print path A and B), 10–11 MPa strength can be reported for plain cement paste (Fig. 2c). Basalt- and glass fiber reinforcement both did not lead to increased flexural strength as compared to plain cement paste, yielding 10 MPa for both types of fibers. Again carbon fiber reinforcement is found to provide the highest increase in flexural strength with values up to 14 MPa. Fig. 3c illustrates that plain cement paste shows similar stress-deformation curves irrespective of the chosen print path (A or B). All tested fibers show post-cracking behavior, if printed via print path B (supplementary material, Fig. S3). However, glass- and basalt fibers show higher residual stress after failure, if fabricated via print path A. A carbon fiber-reinforced cement paste again exhibits a zone of plastic deformation ranging from 0.1 to 0.15% of deformation (orange curve in Fig. 3c).

Since all fibers used in this study exhibit similar tensile strengths and fiber aspect ratios (Table 1), it can be hypothesized, that the low flexural strength values observed for cement samples prepared with glass- or basalt fibers might be connected to the low values of Young's modulus reported for these type of fibers. Samples containing glass or basalt fibers exhibit a cracking behavior which is different to the one shown by non-reinforced reference samples, as shown in the supplementary material (Fig. S3). A residual stress after failure indicates that the hardened cement paste breaks before the glass- or basalt fibers can bear the maximum stress. Consequently, these fiber types will not lead to enhance the maximum flexural strength in the presented 3D-printing technique in the same way carbon fibers will do. However, they still prevent a complete failure of the specimen after first cracks have formed.

Table 2
Flexural strength determined in 3-point bending test for test beams printed along path A and B.

Sample	Print path A [MPa]	Print path B [MPa]
Plain cement paste, (without fibers)	10.6 ± 0.7	11.4 ± 0.6
Fiber-reinforced cement paste (1 vol.-% carbon fibers)	29.1 ± 1.8	13.9 ± 0.5
Fiber-reinforced cement paste (1 vol.-% glass fibers)	12.4 ± 0.8	10.3 ± 0.7
Fiber-reinforced cement paste (1 vol.-% basalt fibers)	13.8 ± 0.5	10.2 ± 0.6

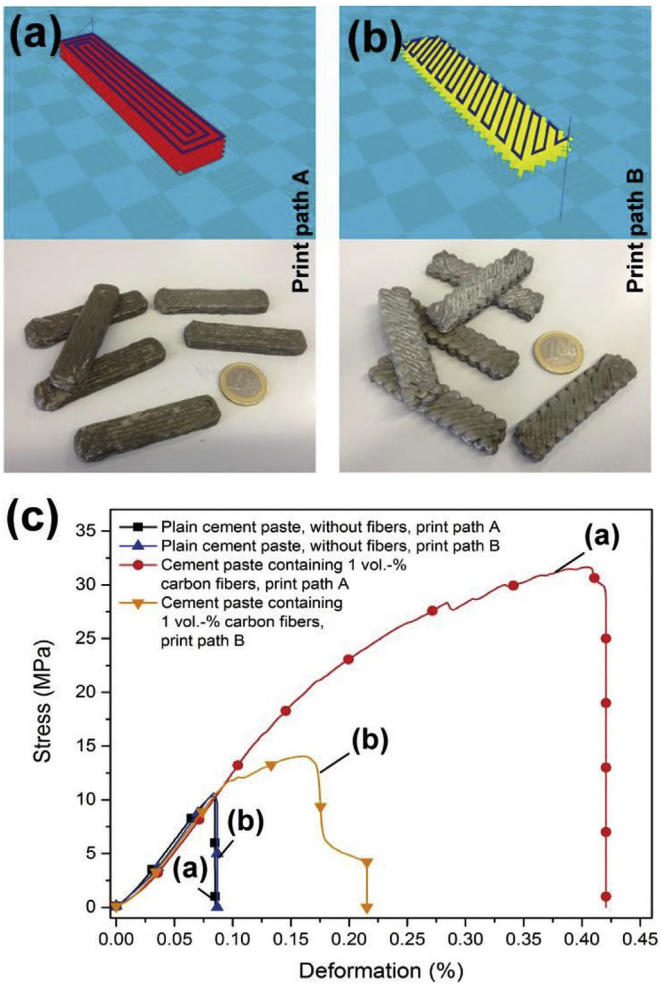

Fig. 3. 3D-print path models in 3D-printing software and photographs of specimens fabricated via (a) print path A and (b) print path B for 3-point bending test. (c) Stress-deformation plots for plain cement samples (without fibers) and carbon fiber-reinforced samples in 3-point bending test proving high flexural strength of print path A samples being reinforced with carbon fibers.

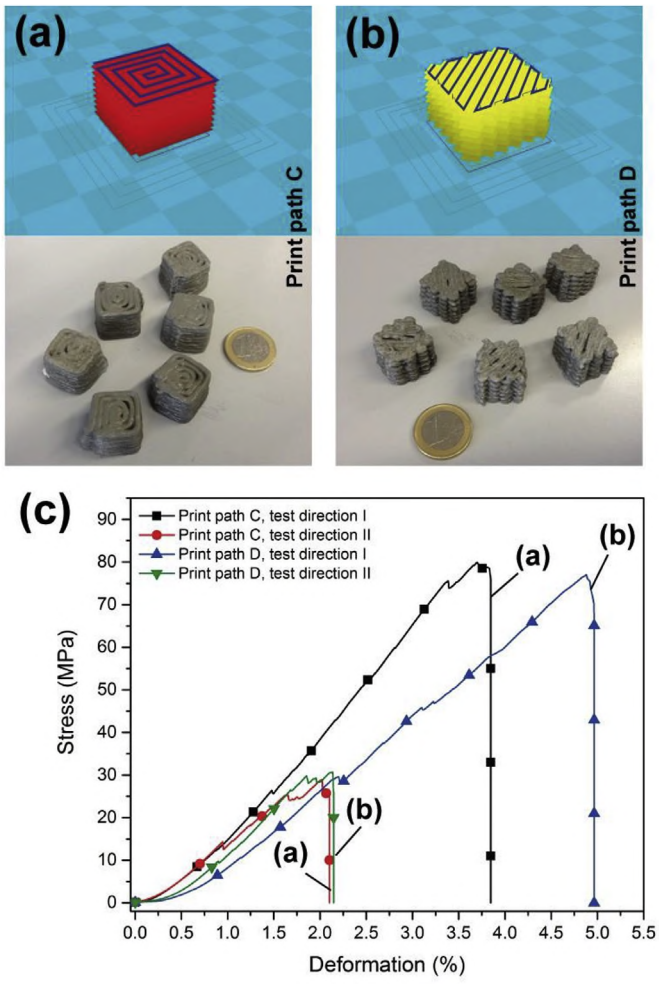

Fig. 4. 3D-print path models in 3D-printing software and photographs of specimens printed via (a) print path C and (b) print path D for uniaxial compressive strength test. (c) Stress-deformation plots for plain cement samples (without fibers) in uniaxial compressive strength test showing high strength for test direction I and low strength for test direction II.

3.1.2. Compressive strength

In compressive strength tests, the cubic tests specimens showed minor dependencies on the fiber material and on the exact print path (C or D) being used. In contrast the direction at which the compressive load was put on the samples has a major influence on the test results. All results are summarized in Table 3 for compressive strength and in supplementary material (Table S2) for deformation modulus in compressive strength test. For each testing series at least 5 specimens were tested. 3D-models and photographs of the prepared specimens are shown in Fig. 4a and b.

Print path C samples (Fig. 4a), being tested in test direction I, exhibit a compressive strength of 80 MPa, for plain cement paste and about 60 MPa for fiber-reinforced test specimens. Different fiber types do not influence compressive strength properties significantly. Stress-deformation diagrams indicate that fiber-reinforced specimens do not show post-cracking characteristics [39] (e.g. resulting from fiber pull-out) in compressive strength test (supplementary material, Fig. S3). If print path C samples are flipped by 90° in the testing setup (test direction II), compressive strength is decreasing to around 30 MPa for all tested samples, no

Table 3
Compressive strength determined in uniaxial compressive strength test.

Sample	Print path C, test direction I [MPa]	Print path C, test direction II [MPa]	Print path D, test direction I [MPa]	Print path D, test direction II [MPa]
Plain cement paste, (without fibers)	81.1 ± 10.0	29.6 ± 10.7	77.9 ± 29.3	30.0 ± 10.8
Fiber-reinforced cement paste (1 vol.-% carbon fibers)	60.6 ± 9.8	27.4 ± 7.9	82.3 ± 26.0	30.8 ± 14.1
Fiber-reinforced cement paste (1 vol.-% glass fibers)	61.0 ± 15.1	20.6 ± 6.8	84.5 ± 22.5	28.1 ± 7.9
Fiber-reinforced cement paste (1 vol.-% basalt fibers)	63.0 ± 15.7	33.7 ± 10.7	85.0 ± 31.2	38.6 ± 15.7

matter if plain or fiber-reinforced cement paste is being used. Reduced compressive strength resulting from separate printing layers is also reported by other authors [13]. Stress-deformation plots show that first cracks form at around 10 MPa, along the printing layers and – since fiber reinforcement is not effective in test direction II – compressive strength is decreasing considerably in comparison to test direction I (supplementary material, Fig. S3). Print path D samples (Fig. 4b) tested in test direction I show compressive strength values of about 80–85 MPa, whereas plain cement paste is performing slightly inferior (80 MPa) in comparison to fiber-reinforced samples (85 MPa). Again, the fiber type does not influence compressive strength significantly. Stress-deformation curves do not show post-cracking characteristics, as presented in Supplementary Material Fig. S3. Print path D and test direction II is resulting in compressive strength values ranging from 30 to 40 MPa, whereas only basalt fibers show slightly higher strength values of 40 MPa. Plain cement paste, carbon- and glass fibers display inferior compressive strength of about 30 MPa. Reduced compressive strength between the printing layers can be reported for print path D, similar to print path C tested in test direction II. Summarizing the results of compressive strength tests, it can be stated that fiber reinforcement, no matter which type of fibers is being used, does not influence compressive strength of the printed cement paste significantly. However, the test direction (parallel or perpendicular to the layers obtained in 3D-printing) has a major impact on the compressive strength, since direction II is resulting in remarkably lower compressive strength than test direction I, no matter which print path is being tested (Fig. 4c).

3.1.3. Density and porosity

The photographs of the 3D-printed specimens (Fig. 3a, Fig. 4a and Supplementary Fig. S4) imply that the samples might exhibit varying porosity, since they were fabricated in layers instead of being casted at once in a mold. Furthermore, no (plate) vibrator has been used for further densification after printing, which could lead to air voids embedded between the layers. The specimen density of each print path sample and a mold-casted reference was measured after drying the specimens in an oven and is given in Table 4. Furthermore the helium porosity of each print path sample and mold casted cement paste was determined by helium pycnometry and is also presented in Table 4. Images of polished cross-sections for all print paths (A to D) and the mold casted specimen are given in the supplementary material (Fig. S4).

The results show, that cement paste printed by print path A exhibits highest specimen density and lowest helium porosity (19.7%). Mold casting and print path C is resulting in slightly lower specimen density and consequently higher helium porosity at 20.2% and 20.3% respectively. In contrast, print path B samples show increased helium porosity at 21.3% and print path D is pushing helium porosity even further up to 22.1%. Since helium gas is used for pycnometry, the determined pore volume contains enclosed air voids (macro pores) and micro pores, which are present in all cement-based binders. All samples were made from the same basic cement paste recipe and mixed the same way, consequently the micro pore volume is identical for all samples. Thus the different helium porosity can be ascribed to a varying amount of macro pores (trapped air voids) induced through 3D-printing. Although flexural strength values can be enhanced by fiber alignment in 3D-printing, porosity may also increase compared to a mold casted sample. Highest porosity was measured for samples exhibiting 3D-printed layers being twisted layer for layer (print path B and D), which is leading to an increased amount of enclosed pores in the fabricated structures. However, if suitable print path configurations are chosen (print path A and C), the porosity of the 3D-printed samples is similar or even lower than those of the mold casted reference.

3.2. 3D-printing of hierarchical materials

Although fiber-reinforced cement paste shows high flexural strength values for optimized print paths (print path A), the development of suitable extrusion systems and customized cement paste compositions [40] make large scale 3D-printed structures expensive, especially if highly priced carbon fibers are being admixed. In order to reduce materials costs, we also investigated the concept of fabricating 3D-printed hollow formworks, which are subsequently filled by common mortar or concrete [41]. The amount of fiber-reinforced infill can be adjusted, depending on the strength needed to ensure the construction's stability. Consequently, these structures are made of (expensive) high flexural strength cement paste, containing aligned reinforcement fibers, and standard mortar or concrete acting as a rather inexpensive filling agent. Filling the voids of the formwork after printing is referred to as *hierarchical structures*. Similar concepts can be found in natural biomaterials: Bone from vertebrates, for instance, displays a hierarchical structure, consisting of a dense and stiff outer layer termed cortical bone and a soft and light core, which is referred to as cancellous bone, thus combining superior mechanical properties and material efficiency in one composite [42–44]. Transferring the principle of hierarchical materials to 3D-printed specimens, a carbon fiber-reinforced cement paste was used for 3D-printing hollow formworks and simple mortar mixture was used to fill the voids in the printed formworks. Thus dense specimens were obtained, which contain varying amounts of a (rather expensive) fiber-reinforced cement paste and a (rather cheap) mortar filling. Since carbon fibers were found to provide the highest increase in flexural strength, this fiber type was used for fiber reinforcement in the fabricated hierarchical structures.

In 3D-printing preparation software the “shell thickness” (in mm) and the amount of material (in vol.-%) in the core of a structure (termed “fill density”) can be adjusted. The borders of the specimens were printed parallel with a shell thickness of 4 mm to create a confining wall, which basically corresponds to a shell of print path A. The core material was printed in a crosshatch pattern, corresponding to a core of print path B, as illustrated in Fig. 5a and b. The described combination of a shell of print path A and a core of print path B is hereafter termed print path E. The fill density for 3D-printing was varied (from 0% to 100% in 25% steps) and the remaining void volume of the specimens was further filled with mortar after printing, in order to adjust the fiber-reinforced cement

Table 4
Specimen density and helium porosity for mold-casted and 3D-printed samples.

Sample	Specimen density [g/cm^3]	Helium porosity [%]
Mold casted cement paste	1.911 ± 0.002	20.2 ± 0.2
3D-printed cement paste, print path A	1.927 ± 0.003	19.7 ± 0.3
3D-printed cement paste, print path B	1.898 ± 0.012	21.3 ± 0.5
3D-printed cement paste, print path C	1.911 ± 0.005	20.3 ± 0.2
3D-printed cement paste, print path D	1.867 ± 0.009	22.1 ± 0.4

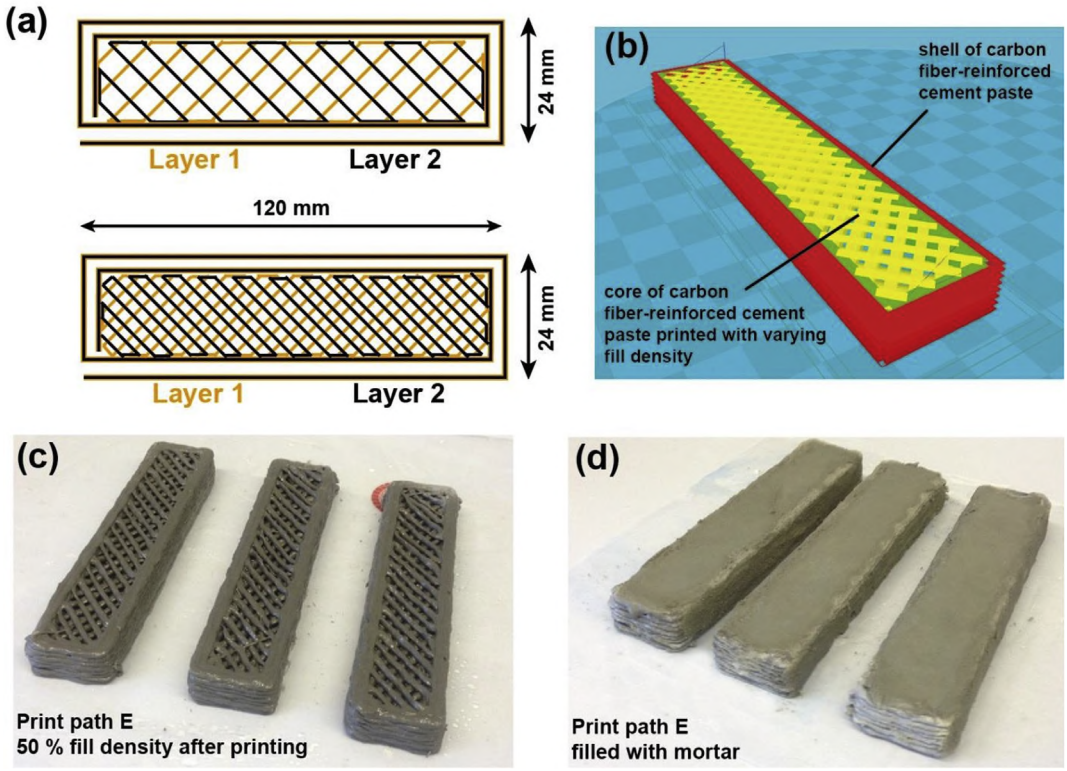

Fig. 5. 3D-printed hierarchical structures. (a) Sketches of "print path E" having a parallel shaped shell and a crosshatch shaped core. By controlling the distance between the single lines of the crosshatch pattern the percentage of fiber-reinforced cement paste in the core area can be adjusted (termed "fill density" in the 3D-printing software). (b) 3D-illustration of print path E for 50% fill density in the core area. (c) Photograph of specimens obtained after 3D-printing (50% fill density) and (d) after loading the structure with mortar.

paste to mortar ratio. For each fill density (0%, 25%, 50%, 75% and 100%) 3 specimens (120 mm in length, 24 mm in width and 12 mm in height) were prepared. Mortar (mixture: 54 % by weight of sand, 36 % by weight of Portland cement, 10 % by weight of water) was poured into the specimens 24 h after printing to fill the whole structures with mortar and thus to obtain compact specimens irrespective of the fill density pre-adjusted for 3D-printing (Fig. 5c, d). Additional illustrations of the print paths and photographs of the specimens before and after filling with mortar are provided in Supplementary Material Fig. S5. The fill density adjusted in 3D-printing preparation software, the weight of the specimens after 3D-printing and the weight after filling with mortar is given in Table 5. Additionally, the ratio of mortar to fiber-reinforced cement paste was calculated and is used to label the samples.

Hollow molds (print path E not being infilled with carbon fiber-reinforced cement paste during printing, 0% fill density) result in a specimen weight of about 30.7 g and were filled after printing with 55.0 g of mortar, resulting in a total specimen weight of 86.7 g. Thus the ratio of mortar to fiber-reinforced cement paste determined to be 1.8 and these samples are referred to as "print path E - 1.8". In an analogous fashion, for the other samples a fiber-reinforced cement paste to mortar ratio of 0.8 can be calculated for print path E with a fill density of 25%, a ratio of 0.4 can be calculated for print path E with a fill density of 50% and a ratio of 0.1 can be calculated for print path E with a fill density of 75%, respectively. Compact reference specimens (not containing any voids) were obtained by adjusting the fill density to 100% in the 3D-printing software. The weight of specimens was determined to be 90.2 g after printing. Since no filling mortar was used the mortar to cement paste ratio was 0 and consequently the specimens are called "print path E – 0". All specimens exhibit almost identical weight (88.0 ± 1.5 g) after filling with mortar, which is proving that most of the (intended) voids

Table 5
Weight of the hierarchical specimens after printing, after filling with mortar and the results of the flexural strength measurement in 3-point bending test.

Sample	Amount of "fill density" adjusted in 3D-printing software [%]	Weight of 3D-printed formwork [g]	Weight after filling with mortar [g]	Ratio of mortar to fiber-reinforced	Flexural strength in 3-point bending test [MPa]
Print path E – 1.8	0	30.7 ± 0.3	85.7 ± 0.6	1.8	12.4 ± 0.5
Print path E – 0.8	25	48.2 ± 0.7	88.8 ± 1.4	0.8	14.4 ± 0.3
Print path E – 0.4	50	65.0 ± 0.3	88.3 ± 0.7	0.4	15.1 ± 0.5
Print path E – 0.1	75	77.2 ± 4.4	87.0 ± 6.5	0.1	16.2 ± 0.3
Print path E – 0	100	90.2 ± 4.4	90.2 ± 4.4	0	17.5 ± 0.5

could be filled with mortar after printing. Flexural strength tests (3-point bending test) were carried out 28 days after fabrication and the results are given in Table 5. Specimen orientation in 3-point bending test was identical to samples tested above and is illustrated in Fig. 2e.

Hollow formwork samples infilled completely with mortar (cement paste to mortar ratio of 0.56) were found to exhibit flexural strength of about 12 MPa. By increasing the fill density in the 3D-printing software, and thus carbon fiber-reinforced cement paste in the core area, flexural strength can be pushed from 12 MPa for "print path E – 01.8" (hollow mold infilled with mortar) to 17.5 MPa for "print path E – 0" (printed at 100% fill density). Table 5 shows, that increasing fill density of fiber-reinforced cement paste in 25% steps is increasing flexural strength in about 1.5 MPa steps, proving that the fill density in the 3D-printing software can be used to control the desired flexural strength of the printed hierarchical specimens. Additional stress-deformation plots are provided in the supplementary material (Fig. S6).

4. Conclusion

In summary, we describe first insights into 3D-printing of fiber-reinforced Portland cement, resulting in a novel composite of cement paste and aligned glass, basalt or carbon fibers. Effective fiber alignment can be reported for the fabricated specimens, leading to a remarkable increase of flexural strength of the composites. Since the printing process was found to enforce an alignment of the fibers along the print path direction, the build path itself was used to spatially control fiber orientation within the printed structures. 30 MPa were found to be the highest flexural strength values achievable by an optimized print path and a content of 1 vol.-% carbon fiber. Other fibers, namely glass- or basalt fibers, were not found to increase flexural strength of the composite significantly. Although the fabricated composites exhibit high flexural strength up to 30 MPa, steel reinforcement would still be necessary for the fabrication of load bearing structures. For a further boost in flexural strength, enabling a complete substitution of steel reinforcement, the development of optimized cement pastes and extrusion systems would be crucially required which are able to print cement pastes containing fiber volume fractions exceeding 1.0 vol.-%. The optimization process will also require a detailed investigation of rheological properties, since e.g. viscosity or yield stress are important parameters to ensure a 3D-printing procedure at high fiber volume contents.

The use of 3D-printing provides access to complex geometries and thus offers the possibility to print hierarchical structures, which have the potential to provide strong and material efficient structures for future constructions. The performed tests on hierarchical specimens demonstrate that these composite types are viable for fine-tuning mechanical properties and consequently could lead to reduced material costs. Further development into more complex 3D-printed structures could include a two-component dispenser system, being able to extrude both plain and fiber-reinforced cement pastes at spatially and temporally varying ratios. A two-component extrusion technique could open up the possibility to fabricate novel structures, exhibiting high (flexural) strength and material efficiency in an automated fabrication process without the need of filling structures manually after 3D-printing. Of course, the fabrication of large constructions (e.g. entire buildings) seems elusive in the near future, since the 3D-printing hardware will have to be adapted to the large-scale processing of Portland cement binders (typically several tons of material per hour) first.

Acknowledgement

The authors wish to thank P. Beroll for recording ESEM images, H. vom Stein for proof-reading the manuscript and the company Toho Tenax for generous supply of carbon fibers.

Appendix A. Supplementary data

TGA measurements, ESEM and optical images, additional stress-deformation-plots and experimental details can be found at http://dx.doi.org/10.1016/j.cemconcomp.2017.02.001.

References

[1] H.-G. Ni, J.-Z. Wang, Prediction of compressive strength of concrete by neural network, Cem. Concr. Res. 30 (2000) 1245–1250.
[2] J.D. Birchall, A.J. Howard, K. Kendall, Flexural strength and porosity of cements, Nature 289 (1981) 388–390.
[3] D.D. Higgins, J.E. Bailey, Fracture measurements on cement paste, J. Mater Sci. 11 (1976) 1995–2003.
[4] R.F. Zollo, Fiber-reinforced concrete: an overview after 30 years of development, Cem. Concr. Comp. 19 (1997) 107–122.
[5] D.D.L. Chung, Carbon Fiber Composites, Butterworth-Heinemann, Newton, 1994.
[6] N. Banthia, J. Sheng, Micro-reinforced cementitious materials, Mater. Res. Soc. Symposium Proc. 211 (1991) 25–32.
[7] P. Morgan, Carbon Fibers and Their Composites, Taylor & Francis, Boca Raton, 2005.
[8] X.Q. Qian, X.M. Zhou, B. Mu, Z.J. Li, Fiber alignment and property direction dependency of FRC extrudate, Cem. Concr. Res. 33 (2003) 1575–1581.
[9] H. Takashima, K. Miyagai, T. Hashida, V.C. Li, A design approach for the mechanical properties of polypropylene discontinuous fiber reinforced cementitious composites by extrusion molding, Eng. Fract. Mech. 70 (2003) 853–870.
[10] B. Mu, M.F. Cyr, S.P. Shah, Extruded fiber-reinforced composites, Advan. Build. Techno. 1 (2002) 239–246.
[11] B. Shen, M. Hubler, G.H. Paulino, L.J. Struble, Functionally-graded fiber-reinforced cement composite: processing, microstructure, and properties, Cem. Concr. Comp. 30 (2008) 663–673.
[12] M. Hambach, H. Möller, T. Neumann, D. Volkmer, Portland cement paste with aligned carbon fibers exhibiting exceptionally high flexural strength (> 100 MPa), Cem. Concr. Res. 89 (2016) 80–86.
[13] T.T. Le, S.A. Austin, S. Lim, R.A. Buswell, R. Law, A.G.F. Gibb, T. Thorpe, Hardened properties of high-performance printing concrete, Cem. Concr. Res. 42 (2012) 558–566.
[14] A. Perrot, D. Rangeard, A. Pierre, Structural built-up of cement-based materials used for 3D-printing extrusion techniques, Mater Struct. 49 (2016) 1213–1220.
[15] E. Lloret, A.R. Shahab, M. Linus, R.J. Flatt, F. Gramazio, M. Kohler, S. Langenberg, Complex concrete structures Merging existing casting techniques with digital fabrication, Comput. Aided Des. 60 (2015) 40–49.
[16] G. Villar, A.D. Graham, H. Bayley, A tissue-like printed material, Science 340 (2013) 48–52.
[17] C.B. Highley, C.B. Rodell, J.A. Burdick, Direct 3D printing of shear-thinning hydrogels into self-healing hydrogels, Adv. Mater 27 (2015) 5075–5079.
[18] B.G. Compton, J.A. Lewis, 3D-Printing of lightweight cellular composites, Adv. Mater 26 (2014) 5930–5935.
[19] J.T. Muth, D.M. Vogt, R.L. Truby, Y. Menguc, D.B. Kolesky, R.J. Wood, J.A. Lewis, Embedded 3D printing of strain sensors within highly stretchable elastomers, Adv. Mater 26 (2014) 6307–6312.
[20] R. Kruger, J. Groll, Fiber reinforced calcium phosphate cements - on the way to degradable load bearing bone substitutes? Biomaterials 33 (2012) 5887–5900.
[21] S. Bose, S. Vahabzadeh, A. Bandyopadhyay, Bone tissue engineering using 3D printing, Mater Today 16 (2013) 496–504.
[22] U. Gbureck, T. Hozel, U. Klammert, K. Wurzler, F.A. Muller, J.E. Barralet, Resorbable dicalcium phosphate bone substitutes prepared by 3D powder printing, Adv. Funct. Mater 17 (2007) 3940–3945.
[23] J.A. Inzana, D. Olvera, S.M. Fuller, J.P. Kelly, O.A. Graeve, E.M. Schwarz, S.L. Kates, H.A. Awad, 3D printing of composite calcium phosphate and collagen scaffolds for bone regeneration, Biomaterials 35 (2014) 4026–4034.
[24] S. Christ, M. Schnabel, E. Vorndran, J. Groll, U. Gbureck, Fiber reinforcement during 3D printing, Mater Lett. 139 (2015) 165–168.
[25] H. Lipson, M. Kurman, Fabricated the New World of 3D Printing, Wiley, Hoboken, 2013.
[26] J. Malda, J. Visser, F.P. Melchels, T. Jungst, W.E. Hennink, W.J.A. Dhert, J. Groll, D.W. Hutmacher, 25th anniversary article: engineering hydrogels for biofabrication, Adv. Mater 25 (2013) 5011–5028.
[27] S.V. Murphy, A. Atala, 3D bioprinting of tissues and organs, Nat. Biotechnol. 32 (2014) 773–785.

[28] R. Bogue, 3D printing: the dawn of a new era in manufacturing? Assem. Autom. 33 (2013) 307–311.
[29] D.D.L. Chung, Dispersion of short fibers in cement, J. Mater Civ. Eng. 17 (2005) 379–383.
[30] T. Sugama, L.E. Kukacka, N. Carciello, D. Stathopoulos, Interfacial reactions between oxidized carbon-fibers and cements, Cem. Concr. Res. 19 (1989) 355–365.
[31] X.L. Fu, W.M. Lu, D.D.L. Chung, Improving the tensile properties of carbon fiber reinforced cement by ozone treatment of the fiber, Cem. Concr. Res. 26 (1996) 1485–1488.
[32] M.J. Shannag, R. Brincker, W. Hansen, Pullout behavior of steel fibers from cement-based composites, Cem. Concr. Res. 27 (1997) 925–936.
[33] A. Abrishambaf, V.M.C.F. Cunha, J.A.O. Barros, The influence of fibre orientation on the post-cracking tensile behaviour of steel fibre reinforced self-compacting concrete, Frat. Integrita Strut (2015) 38–53.
[34] J.A.O. Barros, V.M.C.F. Cunha, A.F. Ribeiro, J.A.B. Antunes, Post-cracking behaviour of steel fibre reinforced concrete, Mater Struct. 38 (2005) 47–56.
[35] V.C. Li, M. Maalej, Toughening in cement based composites .2. Fiber reinforced cementitious composites, Cem. Concr. Comp. 18 (1996) 239–249.
[36] S.P. Shah, C. Ouyang, Mechanical-behavior of fiber-reinforced cement-based composites, J. Am. Ceram. Soc. 74 (1991) 2727–2753.
[37] R.Z. Wang, H.S. Gupta, Deformation and fracture mechanisms of bone and nacre, Annu. Rev. Mater. Res. 41 (2011) 41–73.
[38] H. Kakisawa, T. Sumitomo, The toughening mechanism of nacre and structural materials inspired by nacre, Sci. Technol. Adv. Mat. 12 (2011).
[39] F. Bencardino, L. Rizzuti, G. Spadea, R.N. Swamy, Implications of test methodology on post-cracking and fracture behaviour of steel fibre reinforced concrete, Compos Part B-Eng 46 (2013) 31–38.
[40] T.T. Le, S.A. Austin, S. Lim, R.A. Buswell, A.G.F. Gibb, T. Thorpe, Mix design and fresh properties for high-performance printing concrete, Mater Struct. 45 (2012) 1221–1232.
[41] N. Oxman, J. Duro-Royo, S. Keating, B. Peters, E. Tsai, Towards robotic swarm printing, Archit. Des. 84 (2014) 108–115.
[42] M.A. Meyers, P.Y. Chen, A.Y.M. Lin, Y. Seki, Biological materials: structure and mechanical properties, Prog. Mater Sci. 53 (2008) 1–206.
[43] S. Weiner, H.D. Wagner, The material bone: structure mechanical function relations, Annu. Rev. Mater Sci. 28 (1998) 271–298.
[44] U.G.K. Wegst, H. Bai, E. Saiz, A.P. Tomsia, R.O. Ritchie, Bioinspired structural materials, Nat. Mater. 14 (2015) 23–36.